Refining Constraints on the Origin of Lunar Irregular Mare Patches via Mini-RF and DFSAR Data Analysis

Fei Zhao , Yao Gao , Yanan Dang , Pingping Lu , *Member, IEEE*, Tingyu Meng , *Associate Member, IEEE*, Tianyuan Yang , and Robert Wang , *Senior Member, IEEE*

Abstract—**Irregular mare patch (IMP) is one of the most enigmatic volcanic features in the lunar nearside maria. Their apparently fresh surface morphology and derived young model ages contradict the currently proposed thermal evolution history of the Moon. Lunar orbital synthetic aperture radar (SAR) data of Mini-RF onboard Lunar reconnaissance orbiter and dual-frequency SAR (DFSAR) flying on Chandrayaan-2 are analyzed in this article, to constrain the properties of IMPs within some depth from a radar perspective. The SAR datasets are first orthorectified and coregistered with the optical images, which allow for the interpretation of different terrains in small IMPs. Then, the polarimetric and scattering characteristics of different IMP-associated terrains are extracted and analyzed. Results show that the higher mounds in Ina, Sosigenes and Cauchy-5, as well as the lower uneven units in Ina and Sosigenes IMPs might be covered by a layer of rock-poor materials, which is similar to the surrounding maria regolith. This layer can be as thick as > 0.6 m for the higher mounds and lower uneven units in Ina. Importantly, radar-bright IMPs are found, whose scattering characteristics are similar to these of the rocky units in Ina and the ejecta of degraded craters. Based on the radar characteristics of IMPs, their possible origins and evolution processes are discussed.**

Index Terms—**Dual-frequency synthetic aperture radar (DFSAR), irregular mare patch (IMP), Mini-RF, synthetic aperture radar (SAR), the Moon.**

I. INTRODUCTION

LUNAR irregular mare patches (IMPs) are one of the most mysterious volcanic features because of their anomalously
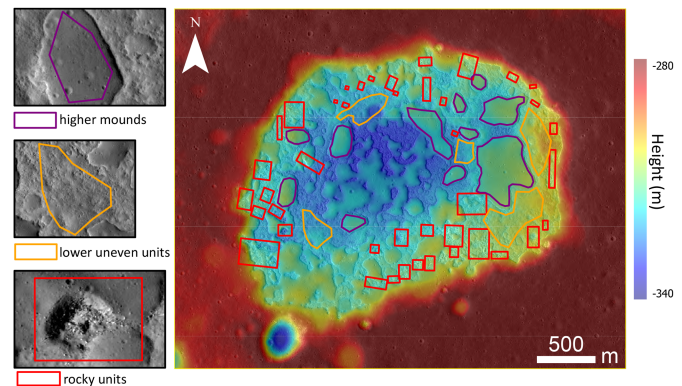
Fig. 1. Three typical terrain types in the Ina structure. Basemap is LRO NAC-derived DTM (NAC_DTM_INACALDER2M) overlain on NAC image (NAC_DTM_INACALDER2M_MOSAIC_60CM).

youthful appearance, i.e., low-density superposed craters, sharp morphology, and highly immature spectral features [1], [2]. Ina was the first IMP discovered during the Apollo era, identified as an irregular depression, with rubbly floors bounded by highly reflective scarps (see Fig. 1). Its inner terrain types can be classified into 3 categories: higher mounds, lower uneven units, and rocky units [3]. Higher mounds are locally higher, optically darker and smooth terrains. Both lower uneven units and rocky units are optically bright depressions, surrounding higher mounds. To date, 91 IMPs, such as Ina, have been identified in the lunar nearside maria [4], [5].

By counting the craters superposed on several IMPs, model ages of younger than 100 Myr were derived for these volcanic features, in contrast to their older host maria ages (~ 1.20–3.73 Ga) [2], [4]. Moreover, the thermal evolution theory of the Moon puts constraints on lunar volcanic activities that they should have ceased at ~ 1.0 Ga ago [1]. In other words, the assessment that IMPs are the product of recent volcanic activity is being questioned. Therefore, what is the actual formation mechanism and post-emplacement process of IMPs? How can they reconcile or definitely disprove the present proposed thermal evolution history of the Moon? Currently, mainly five hypotheses have been proposed as the possible origins for the IMPs: "recent outgassing" [1], pyroclastic eruption [6], lava flow inflation [7],

recent extrusion of basaltic flow [2], and magmatic foam theory [8]. The debate is still ongoing as to which hypothesis is most likely [4], [9].

At present, most of the constraints on IMPs come from the observations of optical and multispectral cameras, which only provide information at the surface ($\sim$1 μm) [1], [2], [3], [4], [7], [10], [11], [12], [13]. After analyzing Ina's Apollo 15 panoramic photograph and Clementine color ratio images, Schultz et al. [1] put forth the theory of "recent outgassing" as the possible explanation for its origin. In this theory, patches of mature lunar regolith would have been recently removed from the Ina structure by the release of volatiles and/or other radiogenic gases, which can account for the well-preserved relief, less superimposed craters, and immature spectral features. With higher resolution albedo ($\sim$0.5 m) and DTM ($\sim$1.2 m) images recently acquired by the narrow angle cameras (NAC) onboard the Lunar reconnaissance orbiter (LRO), a comparison of the unusual mounds in Ina with possible terrestrial analogs led Garry et al. [7] to hypothesize that Ina was formed through lava flow inflation processes. Combined with apprent young model ages of IMPs (i.e., less superposed craters on the higher mounds of IMPs), Braden et al. [2] suggested that the extrusions of basaltic lava flow to form the IMPs must have occurred very recently ($<$ 100 Myr). Alternatively, Wilson and Head [8] proposed the magmatic foam theory for the formation of IMPs. This hypothesis suggested that the lower units were chilled porous lava lake crust, and the higher mounds were formed from the ancient (contemporaneous with the peak period of global lunar volcanism [4]) extrusion of magmatic foams, which were highly vesicular due to the release of volatiles in magmas. This endogenous vesicular characteristic of IMPs made them evolve differently from surrounding maria. Craters were less likely to preserve on them, and developed regolith could be sifted into the underlying voids in the subsurface to refresh the lower units of IMPs. To summarize, the abovementioned hypotheses are only based on the surficial observations. Due to the space weathering effects, original surface characteristics of IMPs can be easily modified, which hinders the speculation about their origin. To validate some of those hypotheses [7], [8], the internal structure information of IMPs is needed.

Thus, robust subsurface properties are required and significant to provide complementary constraints on the origin of lunar IMPs. With the comparatively larger penetration ability of heat flow, the rock abundance (RA) and thermal inertia of several large IMPs within the upper most substrate ($\sim$15 cm) were constrained by Elder et al. [14], Byron et al. [9], and Qiao et al. [11] by using data from the Diviner thermal radiometer onboard LRO. They found that the studied IMPs were slightly rockier, and the thermal inertia of them (except Ina) were higher than that of their surrounding typical mare regolith but lower than that of mare regions with similar RA [9]. Based on the observed low thermal inertial materials at Ina and previous Earth-based radar results (mentioned later), Elder et al. [14] suggested that the removal of material by outgassing or the pyroclastic eruptions were the two hypotheses that could best explain the formation of IMPs. However, they also stated that the possibility that lava

flow inflation or seismic shaking process with magmatic foam theory contributed to the formation of the IMPs could not be precluded. The authors also noted that the certainty of these findings was influenced by the resolution of Diviner, which was comparable to the sizes of those IMPs [9], [14]. Hence, Byron et al. [9] concluded that the observations of Diviner data were consistent with diverging elements of a number of proposed formation hypotheses, and none of them was preferred.

Synthetic aperture radar (SAR) operating in the microwave region can sense deeper into depth ($\sim$0.5–12.5 m) of lunar regolith than optical cameras and thermal radiometer [15]. Available SAR images [16], [17], [18], [19] also have better spatial resolution than Diviner. Therefore, SAR can provide significant constraints on IMPs complementary to other instruments. By using Earth-based SAR data, the pyroclastic eruption hypothesis was proposed by Carter et al. [6] from the observation that low circular polarization ratio (CPR) values were found in the surrounding region of the Cauchy-5 IMP and Hyginus crater [20]. This hypothesis stated that these low-CPR materials were fine-grained pyroclastic deposits. Since this hypothesis is mainly to explain the halos of low CPR surrounding Cauchy-5 and Hyginus, other characteristics (e.g., the apperant young morphology and spectral properties) are yet not addressed by this hypothesis. Furthermore, such a halo of low CPR is not observed near the other IMPs, e.g., Ina [20], [21].

To summarize, in addition to the surface morphology, thermophysical properties of IMPs, and the observed low-CPR halos around some of them, the overall shallow subsurface characteristics of IMPs (especially the different terrain units inside them) are significant to evaluate those hypotheses concerning the formation of them. Different hypotheses on the formation of IMPs may predict different shallow subsurface characteristics, hence different radar observational results can be expected.

For instance, a very thinner regolith at both higher mounds and lower uneven units is expected for the recent extrusion of basaltic flow [14], [22]. The rocks and lava flow can scatter radar waves efficiently [23], [24]. Therefore, both higher mounds and lower uneven units will show enhanced scattering coefficients relative to the surrounding mare regolith in this scenario. In contrast, a layer of rock-poor material covering both higher mounds and lower uneven units presents a more plausible scenario in support of the fine-grained pyroclastic eruption hypothesis [6]. Correspondingly, scattering coefficients of IMPs comparable to or lower than surrounding mare regolith are expected. Moreover, surface scattering will be the dominant scattering mechanism, given the absence of discrete scatterers.

If the recent outgassing hypothesis [1] or magmatic foam theory (with regolith drainage process [11]) is assumed as the formation mechanism of IMPs, little regolith will remain near the gas vents or drainage holes. Since the lower terrains are fresher than the higher mounds [1], [11], the gas vents and drainage holes (if they exist) would most likely to present in the lower units. Consequently, exposed rocks and/or bedrock are expected to appear at the lower units. Then, enhanced radar scattering (especially the volume-scattering component) may be observed at the lower units for the two hypotheses of

TABLE I
GEOLOGIC CONTEXT OF THE STUDIED IMPS

IMP name	Size (m $\times$ m) [a]	Lat (°), Lon (°)	Geologic context	Inner terrains
Ina	3000 $\times$ 1500	18.650, 5.300	small shield volcanic	
Sosigenes	5000 $\times$ 1200	8.335, 19.071	linear rille interior	higher mounds + lower units[b]
Cauchy-5	3000 $\times$ 800	7.169, 37.592	small shield volcanic	
Ross-E-1	1200 $\times$ 200	10.460, 23.547		
Maclear-2	800 $\times$ 270	9.102, 20.298	lunar maria	only lower units[b]
Unnamed #32[c]	255 $\times$ 40	9.102, 20.265		

The location, geologic context and inner terrain types are from [2] and [4]. [a]The size of the IMPs is expressed as D1×D2, where D1 is the maximum length from [4, Table III] and D2 is obtained by dividing the area of IMP by D1. [a]The lower units include lower uneven units where rocks cannot be identified at the surface and blocky units. [a]The unnamed one is the IMP #32 in Qiao et al.'s catalog (Table 3 in [4]).

recent outgassing and magmatic foam theory. However, the radar scattering characteristics of lower uneven units of IMPs would be more complex for the magmatic foam hypothesis. A porous bedrock at lower uneven units is predicted by the magmatic foam theory. The porosity can reduce the effective dielectric constant of bedrock. In addition, the regolith sifting process could also smooth the surface of IMPs [11]. Therefore, there is also the possibility that the lower uneven units of some IMPs will show scattering coefficients significantly lower than those of rough cohesive bedrock. As for the higher mounds in IMPs, a layer of thick regolith may align with the magmatic foam theory, but its relevance to the outgassing hypothesis is less clear, contingent upon the volume of redeposited regolith (most likely to be minimal). Keeping these in mind, radar can distinguish between regolith fines and rocks in the shallow subsurface of different terrain units in IMPs, thereby helping to refine and constrain diverse hypotheses regarding their formation mechanism.

In this article, we quantitatively analyze orbital SAR data to characterize IMPs (including those that have never been studied before by SAR). Not only the CPR, but also the polarimetric properties, and scattering coefficients of IMP-associated features and terrains (when they are resolvable) are studied, aiming to provide valuable insights into the origin of lunar IMPs from a radar perspective.

II. MATERIALS AND METHODS

The datasets and context of IMPs studied in this article are briefly described first. Then, the flow of data processing and methods of analysis are detailed.

A. Datasets and Study Regions

Most of the IMPs are very small. The size of the second largest IMP Ina is only $3000 \times 1500 \,\mathrm{m}^2$ (see Table I). The smallest IMP studied in this article (ranked as the 32nd largest among the 91 IMPs in the catalog of [4]) has a size of only $255 \times 40 \,\mathrm{m}^2$. Furthermore, the terrain units within IMPs are of even smaller scale. For instance, the majority of the isolated higher mounds

in Ina measure around 150 to 350 m in length along their main axis, while some of the larger standablone mounds extend between 500 and 600 m. The minor axis generally ranges from 100 to 200 m, resulting in an elongated shape for these higher mounds [7]. As a comparison, the resolutions of avaliable Earth-based P-band [25] and S-band [26] SAR data are 400 and 80 m, respectively. Therefore, robust radar characteristics of small IMPs and specified isolated terrain units cannot be retrieved from these data. Instead, the high-resolution data from orbital SAR Mini-RF (S-band, 2.38 GHz) [27] onboard LRO and DFSAR (L-band, 1.25 GHz) [17] onboard Chandrayaan-2 are utilized in this study. The azimuthal × slant-range resolution of Mini-RF and dual-frequency SAR (DFSAR) are $15\mathrm{m} \times 23\,\mathrm{m}$ and $24\,\mathrm{m} \times 20\,\mathrm{m}$, respectively.

Mini-RF is a compact polarimetric SAR, which transmits circularly polarized waves and receives two orthogonal linear-polarized waves. If the transmitted wave is left-circularly polarized (as the data used in this article), the received information can be fully represented by the Stokes vector [28]

$$\mathbf{I} = \begin{bmatrix} I_1 \\ I_2 \\ I_3 \\ I_4 \end{bmatrix} = \begin{bmatrix} \left\langle |E_{HL}|^2 + |E_{VL}|^2 \right\rangle \\ \left\langle |E_{HL}|^2 - |E_{VL}|^2 \right\rangle \\ 2\mathrm{Re}\left\langle E_{HL}E_{VL}^* \right\rangle \\ -2\mathrm{Im}\left\langle E_{HL}E_{VL}^* \right\rangle \end{bmatrix} \quad (1)$$

where I_1, I_2, I_3, and I_4 are the Stokes parameters, E_{HL} and E_{VL} are the amplitudes of received horizontal(H)- and vertical(V)-polarized waves, respectively. The bracket $\langle \cdot \rangle$ indicates ensemble averaging, and superscript $*$ denotes the conjugate operator.

DFSAR is a full-polarimetric SAR, which transmits and receives both H- and V-polarized waves, hence containing complete polarimetric information [17], [29].

Taking the locations of 91 IMPs in the catalog of Qiao et al. [13] as input, we checked whether the specified IMP was encompassed by the footprints of Mini-RF and/or DFSAR. If the IMP was covered, then corresponding SAR images were projected and coregistered with the optical images. Then, based
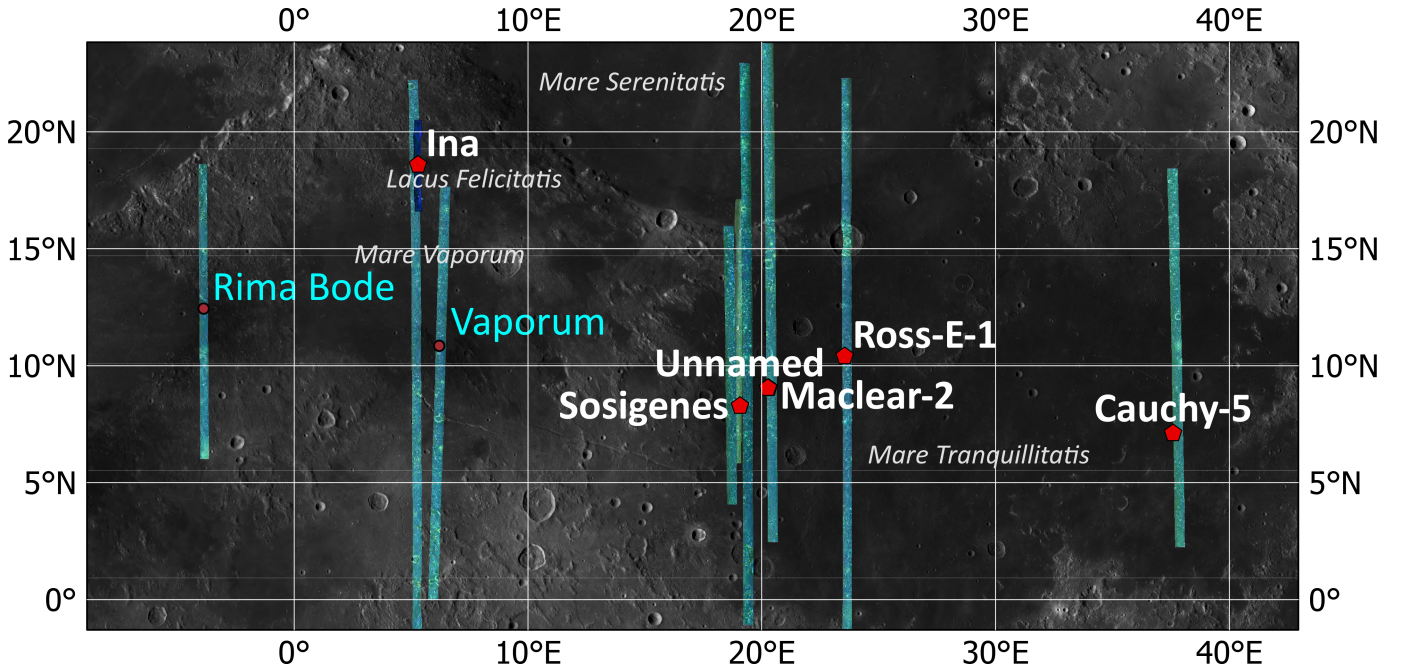
Fig. 2.   Locations of studied IMPs and pyroclastic deposits. Mini-RF and DFSAR (only for Ina) m-chi decomposition RGB images are overlain on LRO WAC 100 m mosaic.

on the total-power SAR image of IMP, we manually checked whether the IMP could be identified confidently. In this process, these IMPs that were covered by SAR data but cannot be identified from the SAR images were generally very small (with maximum lengths < 200 m). After extensive screening, 6 IMPs were selected. Their geolocations are illustrated in Fig. 2 with corresponding m-chi [30] polarimetric decomposition images of Mini-RF and DFSAR overlain on the LRO wide angle camera (WAC) 100 m mosaic map [31]. The sizes, geological contexts and inner terrain types of each selected IMP [4] are summarized in Table I. Note that the selected IMPs (except the unnamed #32) are relatively large ones (with maximum lengths > 800 m versus those of most others in the IMPs catalog [4] < 400 m). The tiny unnamed #32 (see Table I) is merged with Maclear-2 in subsequent analysis, due to its proximity and similarity to Maclear-2.

To reevaluate the pyroclastic eruption hypothesis, two typical pyroclastic deposits [i.e., Rima Bode (3.872° W, 12.442° N) and Vaporum (6.206° E, 10.850° N) [32], as shown in Fig. 2] are also included for comparison with the materials in IMP. Pyroclastic deposits on the Moon are generally composed of fine-grained materials, and appear to be dark in both optical and radar images [32]. Due to the lack of embedded rocks, pyroclastic deposits are also characterized by low CPR values [6], [32].

The product IDs of the datasets used here are listed in the supporting document attached to this article.

B. Data Preprocessing and Polarimetric Analysis

It is well known that the existing Mini-RF map-projected monostatic radar data available from the Planetary Data System

(PDS) have noticeable cross-track and along-track offsets caused by topographic parallax and timing error, respectively. [33], [34], [35], [36]. When dealing with IMPs, it is crucial to ensure proper orthorectification and coregistration of the SAR data due to their small sizes. The level-1 Mini-RF datasets in slant range-azimuth coordinate were downloaded and then orthorectified using USGS integrated software for imagers and spectrometers [37]. In this process, the LRO LOLA DEM data with resolution of 1024 pixels per degree (PPD) were incorporated to provide the topography of the Moon [38]. Then, the orthorectified images were manually registered with Kaguya terrain camera (TC) gridded images [39] and/or LRO NAC [40] images in ArcGIS Pro, to compensate for the residual offsets. The range-doppler geolocation algorithm [41] was implemented to orthorectify and geocode the DFSAR data. The LOLA DEM and satellite position data extracted from corresponding DFSAR geometry grid files were used to solve the range-doppler equation.

The dominant radar scattering mechanisms of targets are highly correlated with their morphology and structure. To visualize the dominant scattering mechanisms of IMPs, the m-chi polarimetric decomposition is adopted. The double-bounce, single- and volume-scattering power are determined from the following equations [30]:

$$P_d = \sqrt{mI_1\left(1 \pm \sin 2\chi\right)} \qquad (2)$$

$$P_s = \sqrt{mI_1\left(1 \mp \sin 2\chi\right)} \qquad (3)$$

$$P_v = \sqrt{\left(1 - m\right)I_1} \qquad (4)$$

where $m = \sqrt{I_2^2 + I_3^2 + I_4^2}/I_1$ is the degree of polarization, and $\chi = 0.5 \arcsin[-I_4/(mI_1)]$ is the ellipticity angle of the

completely polarized component of the backscattered wave. The P_d, P_s, and P_v are used as red (R), blue (B), and green (G) channels for rendering the pseudocolor images, respectively. The upper sign in the $\pm$ and $\mp$ symbols is employed for left circular transmitting, whereas the lower sign is used for the right circular transmitting. The advantage of m-chi adopted here over m-delta decomposition [42] is that the parameters it depends on are roll-invariant, so the results would not be confused by the topography.

For the full-polarimetric DFSAR data, the compact-polarimetric data (i.e., the Stokes parameters) can be synthesized, and then the m-chi decomposition can be employed. Furthermore, the Yamaguchi 4-component full-polarimetric decomposition with rotation compensated (Y4R) [43] is implemented for DFSAR data to validate the results of m-chi decomposition.

C. Quantitative Analysis of the Scattering Characteristics

To compare different IMP-associated terrains and other materials (such as pyroclastic and impact ejecta) in different regions, it deserves a quantitative statistical analysis of their scattering characteristics. Therefore, different terrains in IMPs and their surrounding regions were sketched carefully and conservatively according to the high-resolution NAC or TC images, which ensured that the statistic characteristics of the current unit were not contaminated by adjacent geologic units.

Moreover, the inherent speckle noise on SAR data should be suppressed to obtain robust statistics of the polarimetric parameters of targets [29]. One of our goals is to study the radar characteristics of different terrain units in IMPs, which are generally tiny structures, hence texture-maintaining filtering algorithm should be used. Under this consideration, the nonlocal polarimetric filter NLSAR [44] was employed to reduce the impact of speckle noise.

To characterize the IMPs, the opposite-sense (OC) and the same-sense circularly (SC) polarized scattering coefficients can be calculated from the Stokes parameters [15]

$$\sigma_{OC}^0 = 0.5\,(I_1 \pm I_4) \tag{5}$$

$$\sigma_{SC}^0 = 0.5\,(I_1 \mp I_4) \tag{6}$$

where the symbols $\pm$ and $\mp$ should be interpreted according to the conventions defined in (2) and (3). σ_{OC}^0 is the polarized component of the backscattered power, which is expected from single scattering of a flat surface. The strength of σ_{OC}^0 is significantly influenced by incident angles, and is sensitive to the dielectric constant (or composition and bulk density) and roughness of the IMPs [45]. σ_{SC}^0 represents the depolarized scattering power. When the surface becomes rougher and/or scatterers like rocks suspended within the regolith, the σ_{SC}^0 will increase [15]. The ratio between them, i.e., CPR $= \sigma_{SC}^0/\sigma_{OC}^0$, is a widely used parameter in the field of planetary science to characterize the roughness and rockiness of geological targets [23], [46], [47], [48]. In this study, only σ_{OC}^0 and CPR are selected for the quantitative analysis, because other polarimetric parameters are correlated with them or are not sensitive to the studied geologic targets here.

III. RESULTS

The scattering mechanisms of different terrains in Ina, Sosigenes, Cauchy-5 and those of other three IMPs (only containing lower uneven units) are analyzed sequentially. Then, the radar scattering characteristics of different IMP-associated terrains are quantitatively compared. These results will serve as the basis for discussing the origin of IMP in the next section.

A. Radar Characteristics of Different Terrains in Ina, Sosigenes and Cauchy-5

As shown in Figs. 1 and 3(a), the inner terrain types of Ina can be classified into 3 categories: higher mounds, lower uneven units, and rocky units. Higher mounds are locally higher, optically darker, and smooth terrains, and they might be the product of magmatic extrusion or redeposited regolith as predicted by different origin hypotheses. Both lower uneven units and rocky units are optically bright depressions, surrounding the higher mounds.

The Mini-RF total power image (i.e., the Stokes parameter I_1) is shown in dB scale in Fig. 3(b). At a first glance, the bright regions match well with the rocky units outlined with red boxes. This is more obvious in the linear-scale stretched images in Fig. S1 of the Supplementary Material. Many small facets made up of rocks can reflect microwave energy directly, resulting in brighter features than the surrounding terrain. The rocky units mainly appear in the peripheral areas inside Ina. From the total power image of DFSAR L-band data [see Fig. 3(c)], similar conclusions can be drawn. Noting that the DFSAR illuminates Ina from the east to the west, the western inner wall of Ina is much brighter than its eastern wall. However, for the central part of Ina, there are spots (related to lower units) as bright as rocky units in the DFSAR image [see Fig. 3(c)], but only faint boundaries between lower units and higher mounds can be identified in the Mini-RF image [see Fig. 3(b)].

In order to determine the cause of the bright spots at the center of Ina in Fig. 3(c), the cross-pol and the ratio of cross-polarized to copolarized images from DFSAR for Ina are shown in Fig. 3(d) and (e), respectively. The ratio of cross-pol to co-pol image is calculated as $R = 2\sigma_{HV}^0/(\sigma_{VV}^0 + \sigma_{HH}^0)$ [19]. The cross-polarized backscattering coefficient σ_{HV}^0 is less influenced by the topography (e.g., the oriented facets that face radar), and hence is a good indicator of diffuse scattering caused by rocks. In the σ_{HV}^0 image [see Fig. 3(d)], the bright spots are mainly distributed in the peripheral areas inside Ina, which is consistent with the results of I_1 image of Mini-RF [see Fig. 3(b)]. This observation proves that those bright spots at the central part of Ina in the DFSAR SPAN image [see Fig. 3(c)] might be the edges of higher mounds being blurred due to imperfect orthorectification, which is consistent with the steep slopes at the junction of higher mounds and lower units. The ratio of cross-pol to co-pol R image [see Fig. 3(e)] shows relatively enhanced values mainly at the eastern inner wall of Ina, where the local incidence angles are larger (noting that the DFSAR illuminates Ina from the east to the west again) and the diffuse scattering component becomes important. Combined with the polarimetric decomposition images Fig. 3(g)–(i), which show dominant surface scattering (blue) at the center of Ina, the
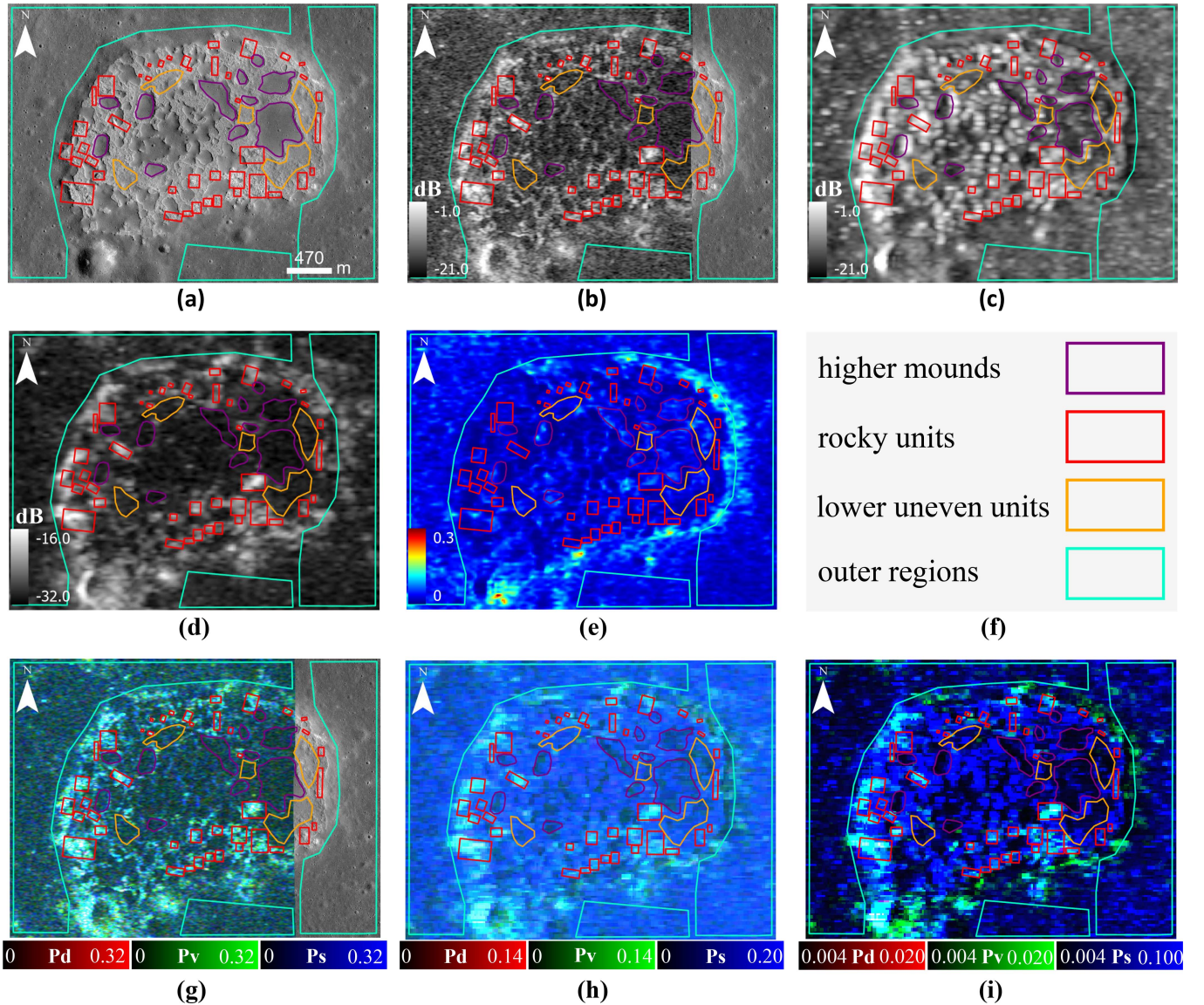
Fig. 3. Images of Ina with its inner floor higher mounds, lower uneven units, rocky units and surrounding regions outlined by purple, brown, red, and cyan lines, respectively. (a) LRO NAC image (NAC_DTM_INACALDER2M_MOSAIC_60CM). (b) Total power image I_1 from Mini-RF. (c) Total power image (span) from DFSAR. (d) Cross-polarized image σ^0_{HV} from DFSAR. (e) Ratio of cross-polarization to copolarization image R derived from DFSAR. (f) Legend for other subplots. (g) m-chi decomposition image from Mini-RF. (h) m-chi decomposition image from DFSAR. (i) Y4R decomposition from DFSAR. RGB images should be interpreted as R = double-bounce scattering power, G = volume scattering power and B = surface/odd scattering power.

possibility that these spots are detected rocks in the subsurface is also less likely.

From Fig. 3(b)–(d), another significant result can be observed. Both lower uneven units and higher mounds appear dark as the surrounding mare regolith in these images. Moreover, the R values of higher mounds [see Fig. 3(e)], and lower uneven units in Ina and surrounding maria regions are less than 1/3, which indicates dominant surface scattering [19]. Fig. 4(b) and (d) shows the scattering intensity I_1 image of Sosigenes and Cauchy-5 IMPs. The main observations can be summarized as follows.

1) Both the higher mounds and lower units in Sosigenes have backscattering coefficients as low as those of surrounding maria regolith.

2) The higher mounds in Cauchy-5 also show low backscattering coefficients.

3) The lower units spread sporadically on the north shield flank of Cauchy-5 depression, and have enhanced backscattering coefficients.

In summary, the weak scattering characteristics observed in higher mounds and lower uneven units in Ina, Sosigenes, and higher mounds in Cauchy-5 suggest the presence of materials with a low dielectric constant in these terrain units, accompanied by a low level of surface roughness.

To further investigate the physical properties of different terrains in IMPs, m-chi decomposition is employed on Mini-RF data [see Fig. 3(g)] and DFSAR synthesized Stokes data [see Fig. 3(h)] of Ina. The available SAR images encompassing
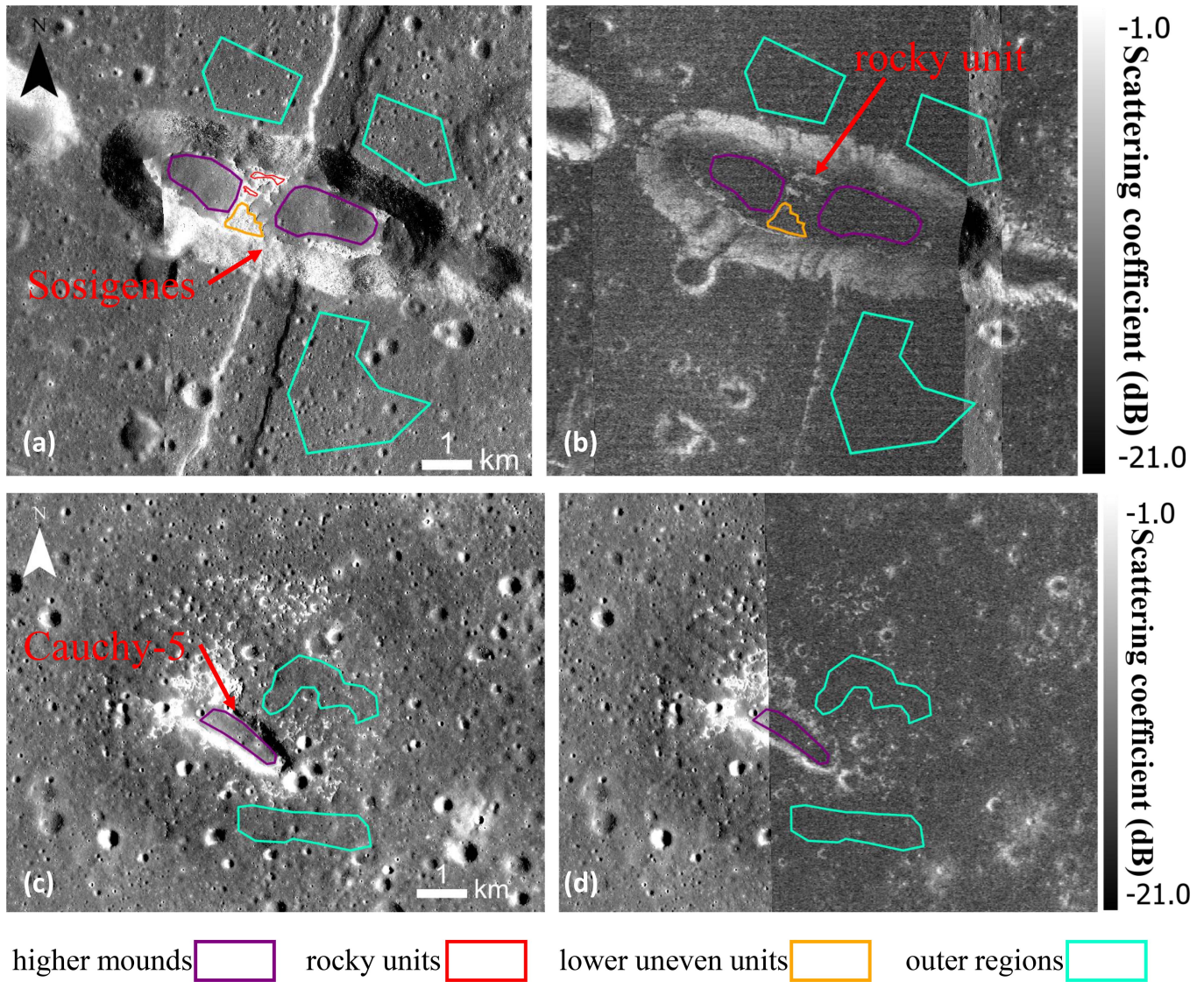
Fig. 4. Optical and SAR images of Sosigenes and Cauchy-5. (a) NAC optical image of Sosigenes (M192824968LE, M192824968RE, NAC_DTM_SOSIGENES01_M1129354261_120CM). (b) Mini-RF total power I_1 image of Sosigenes. (c) NAC optical image of Cauchy-5 (NAC_DTM_CAUCHY_M1108025067_130CM). (d) Mini-RF total power I_1 image of Cauchy-5.

Sosigenes and Cauchy-5 exhibit polarimetric distortion, characterized by unusually high CPR values (with a mean value 0.98) in Sosigenes and a CPR gradient across the range dimension in Cauchy-5 (see Fig. S3 of the Supplementary Material). In Fig. 3(g) and (h), the rock units are mainly green to white, indicating dominant random volume scattering and/or complex mixed scattering mechanisms. Again, lower uneven units and higher mounds are indistinguishable from mare regolith, and all of them are dominated by surface scattering (blue). It is also observed that the m-chi decomposition image of Mini-RF is generally slightly greener than that of DFSAR. After comparing many images within different scenes, we find that this discrepancy between Mini-RF and DFSAR is a systematical phenomenon. As a preliminary thought, the variance may be due to Mini-RF having a shorter wavelength (12.6 cm compared with DFSAR's 23.0 cm) and a higher incident angle (50.1° versus

19.6°). Specifically, there may be centimeter-sized small rocks sensed by Mini-RF but not DFSAR, and/or higher-order scattering with randomness becomes significant at a large angle of incidence. Both two factors can make m-chi images of Mini-RF greener. Finally, the result of full-polarimetric decomposition Y4R [see Fig. 3(i) is consistent with that of m-chi [see Fig. 3(h)].

Based on the analysis presented, it can be inferred that a layer of materials with a low dielectric constant (e.g., rock-free regolith fines) must exist in the shallow subsurface of higher mounds and lower uneven units in IMPs. At least, the RA of these two types of terrain in Ina, Sosigenes, and higher mounds in Cauchy-5 are comparable to those of surrounding mare regolith. This conclusion can be evidenced from few excavated rocks near the impact craters atop higher mounds (see Fig. S2 of the Supplementary Material) [2], [10]. According to the morphology of small craters on the lower uneven units

TABLE II
MINI-RF RADAR CHARACTERISTICS AND THERMAL PHYSICAL PROPERTIES OF IMPS

IMP name	Terrain units	σ_{OC}^{0} (dB): median±std.	CPR: median±std.	RA (%)[a]	H (m)[b]
Ina	higher mounds	−18.37±1.49	0.39±0.10	0.39	0.131
	lower uneven	−17.70±1.47	0.38±0.11	0.65	0.143
	rocky units	−10.55±3.76	0.40±0.19	/[c]	/[c]
	outer regions	−16.31±1.25	0.34±0.07	0.36	0.078
Sosigenes	higher mounds	−18.04±1.93	/[d]	0.85	0.046
	lower uneven	−16.98±2.13	/[d]	1.57	0.047
	rocky units	−12.46±2.47	/[d]	/[c]	/[c]
	outer regions	−18.14±2.00	/[d]	0.76	0.070
Cauchy-5	higher mounds	−17.43±1.84	/[d]	1.11	0.067
	outer regions	−17.18±1.65	/[d]	0.46	0.071
Ross-E-1	lower units[e]	−10.69±1.84	0.34±0.10	1.70	0.060
	outer regions	−16.45±1.04	0.37±0.05	0.46	0.069
Maclear-2	lower units	−10.03±1.77	0.36±0.10	1.99	0.070
and Unnamed[f]	outer regions	−15.92±0.52	0.38±0.03	0.37	0.072

[a,b]The RA and H-parameter values of inner terrain units [higher mounds, lower (uneven) units] are from Table 2 in [9]; The RA and H values of outer regions surrounding Ina, Sosigenes and Cauchy-5 are from [14, Tables I and II]. The RA and H values of outer regions surrounding Ross-E-1 and Maclear-2 are calculated in this study based on the global RA map [50] and H-parameter map [51]. [c]It is difficult to obtain robust RA and H values of those tiny terrains. However, elevated RA values (> 1.0%) are correlated to those units based on the global RA map. [d]Due to poor polarimetry data quality, meaningful and accurate CPR values cannot be calculated. [e]The lower units include lower uneven units where rocks cannot be identified at the surface and blocky units. [f]The Unnamed one is the IMP #32 in Qiao et al.'s [4] catalog.

of Sosigenes, Qiao et al. [10], [11] suggested that these units might be mantled by a layer of unconsolidated materials as thick as <∼ 1.5–2.5 m, which is also consistent with our results. However, the Diviner data reveal that the RA values of the higher mounds in Sosigenes and Cauchy-5, as well as the lower uneven units in Ina, Sosigenes, and Cauchy-5 are significantly higher than those of their respective surrounding regions (see Table II). In other words, the results of the Diviner indicate that the higher mounds and lower uneven units in IMPs are rockier than the surrounding maria regions [9], contradicting the conclusion drawn from SAR data. This discrepancy between the results of Diviner and SAR may arise from the potential contamination of Diviner measurements on higher mounds and lower uneven units by adjacent rocky units, due to its coarse resolution (238 m).

Furthermore, we compare Mini-RF SAR polarimetric decomposition images of Ina with the two typical fine-grained pyroclastic deposits, i.e., Rima Bode and Vaporum (see Fig. 5). Similar to Ina, the pyroclastic deposits also display a dark and blue color, indicating weak scattering and dominant surface scattering mechanism. This result may support the presence of fine-grained materials (e.g., pyroclastic deposits) at the higher mounds and lower uneven units in Ina. In addition, within certain areas of the pyroclastic deposits, the blue color is purer, suggesting a smoother and more homogeneous characteristic in those regions.
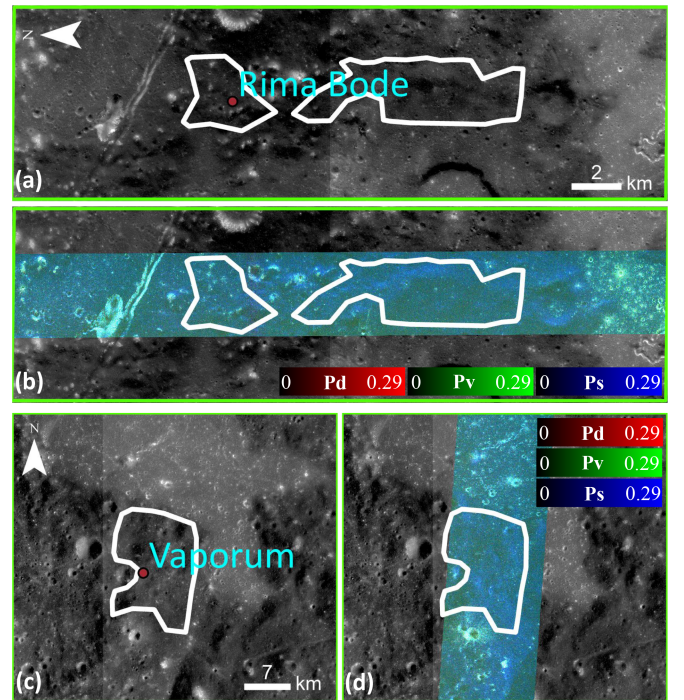

Fig. 5. (a) TC optical image (TCO_MAPs02_N15E354N12E357SC, TCO_MAPs02_N12E354N09E357SC) and (b) m-chi decomposition image of Rima Bode. (c) TC optical image (TCO_MAPs02_N12E006N09E009SC, TCO_MAPs02_N12E003N09E006SC) and (d) m-chi decomposition image of Vaporum. Pyroclastic deposits as outlined by white lines.
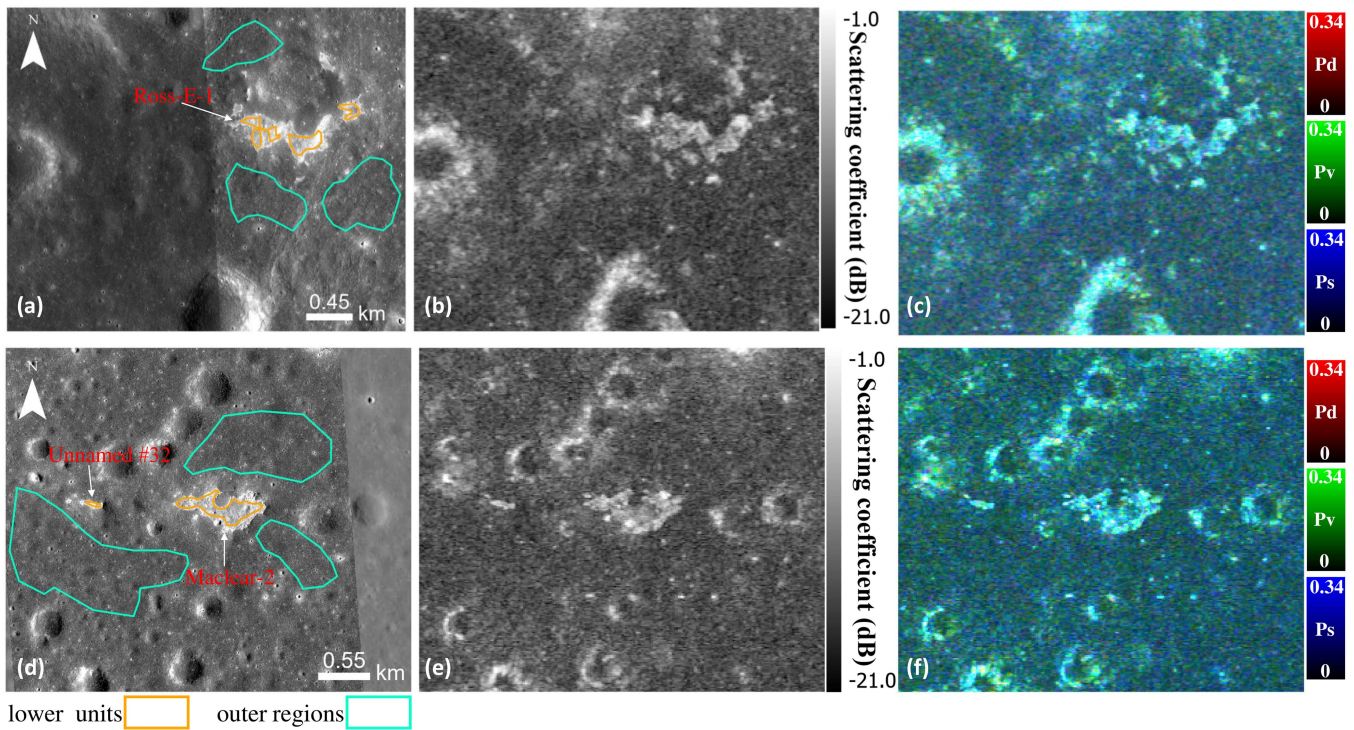
Fig. 6. Radar-bright IMPs. (a) NAC optical image (M1279955333LE, M1279955333RE). (b) Mini-RF total power I_1 image and (c) m-chi decomposition image of Ross-E-1. (d) NAC optical image (M1378662549RE). (e) Mini-RF total power I_1 image and (f) m-chi decomposition image of Maclear-2 and the Unnamed #32.

B. Radar Bright IMPs: Ross-E-1, Maclear-2 and the Unnamed #32

Most of the IMPs (86 out of 91) classified as Class #2 by Qiao et al. [4] host only lower units (uneven or rocky units), while lack higher mounds like those found in Ina. These IMPs are generally small, which suggests that a large volume of materials were involved in the development of the raised mounds. Among this class of IMPs, several IMPs are covered by the footprints of Mini-RF but only the largest two, i.e., Ross-E-1 and Maclear-2 (also the unnamed #32) can be identified from the SAR images.

Interestingly, compared to the darkness of the main part of Ina [see Fig. 3(b) and (d)], Ross-E-1 [see Fig. 6(b)], Maclear-2 and the unnamed #32 [see Fig. 6(e)] are locally bright features, resembling the ejecta and/or rim of nearby craters [e.g., a degraded crater at the west of Ross-E-1 in Fig. 6(b)]. However, few rocks can be identified on their surface from NAC optical images [see Fig. 6(a) and (c)]. This radar-bright characteristic can be caused by the rocks on these IMPs. From the enlarged NAC images of Ross-E-1 and Maclear-2 (see Figs. S5 and S6 of the Supplementary Material, sparse rocks can be identified. In addition, many bright spots exist in these NAC images, and are likely related to gravel fields, where the rocks are too small and cannot be resolved by the NAC. Furthermore, the patches of Ross-E-1 and Maclear-2 in m-chi decomposition images show compound scattering mechanisms of high randomness and are very similar to the inner wall (where small surface rocks can be readily replenished) and ejecta of nearby craters. A quantitative analysis of both radar characteristics and thermal

physical properties of these IMPs provides additional support for the interpretation presented here.

To conduct a more comprehensive analysis of the surface characteristics of these radar-bright IMPs, we use the phase-ratio technique [11], [49] to characterize their surface roughness at subresolution scale of NAC images. The rougher the surface is, the less sensitive its apparent albedo $f(\alpha)$ is to the phase angle α of optical images. We follow the method of Qiao et al. [11], and put the NAC image with smaller α in the numerator and larger α in the denominator. To avoid the impact of topography, the selection of paired NAC images prioritizes those with similar solar azimuth angles. The derived phase-ratio images are displayed in Fig. 7. Beyond the areas where rocks can be identified in the enlarged NAC images (see Figs. S3 and S4 of the Supplementary Material), the radar-bright IMPs exhibit relatively low phase-ratio values compared with their surrounding regions. Therefore, these IMPs may be mantled by a layer of materials with significantly lower subresolution roughness. In addition, the phase-ratio images also reveal that the materials with lower subresolution roughness in these IMPs [especially the Maclear-2, Fig. 7(b)] have confined (not diffuse) extents. This finding aligns with the characteristics observed in the lower uneven units of Sosigenes and Ina [10], [11], where the subresolution roughness is also notably smoother than that of their surrounding regions.

The smoother subresolution roughness of Ross-E-1, Maclear-2, and Unnamed #32 compared with the surrounding regions is unexpected from their larger radar scattering coefficients. This contrast suggests that the fine-grained materials covering the
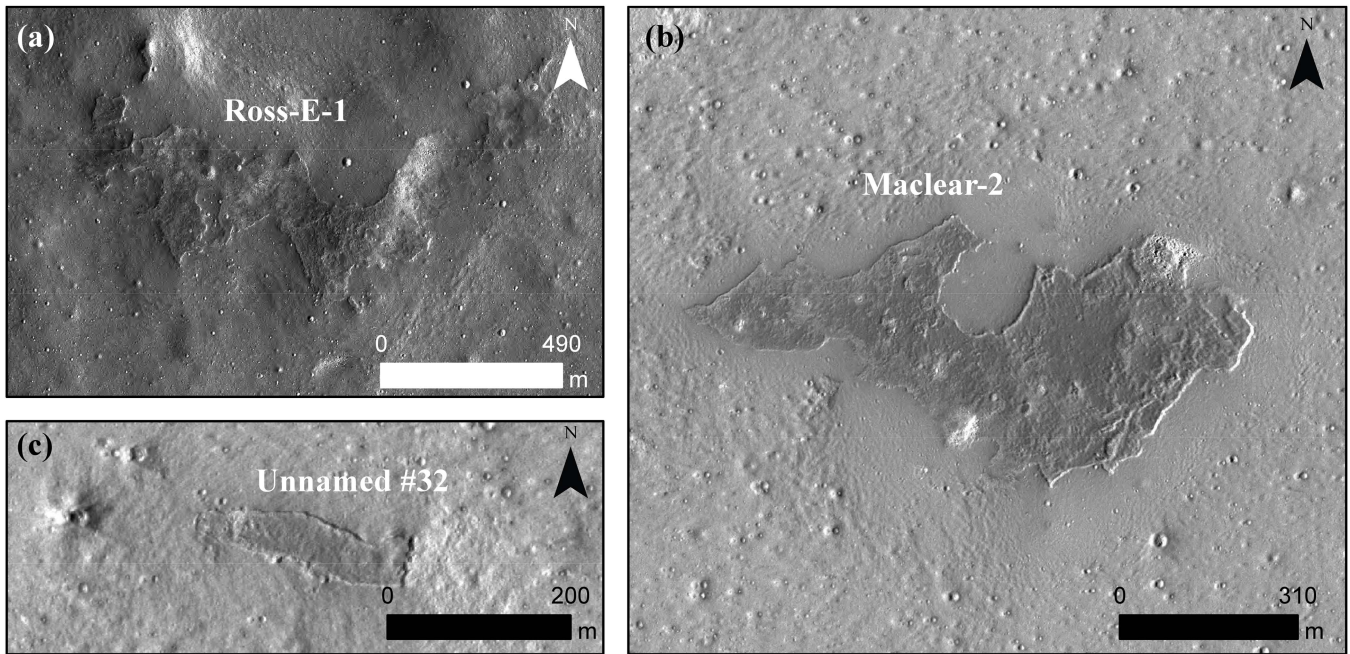
Fig. 7.　LRO NAC phase-ratio images of the radar-bright IMPs. (a) $f(37°)/f(64°)$ of Ross-E-1 (M1391556637LE, M1319918900LE), stretched from 1.5 to 3.0. (b) $f(22°)/f(59°)$ of Maclear-2 (M1212932755RE, M1212946821RE), stretched from 1.0 to 2.0. (c) $f(22°)/f(59°)$ of unnamed #32 (M1212932755RE, M1212946821RE), stretched from 1.0 to 2.0.

radar-bright IMPs are exceptionally thin, significantly thinner than those observed in Sosigenes and Ina. Thus, these thinner materials allow the IMPs to exhibit a smoother appearance without causing substantial radar scattering attenuation.

C.　Quantitative Characteristics of IMPs

To obtain quantitative radar characteristics of IMPs, we outline different terrains in IMPs and their surrounding regions. Higher mounds, lower uneven units, rocky units and surrounding mare regions are labeled by purple, brown, red, and cyan lines respectively (see Figs. 3 and 6). By drawing each region conservatively and excluding small units, robust and unambiguous statistics of each type of terrain are guaranteed. σ_{OC}^0 and CPR of selected IMPs, pyroclastic deposits (see Fig. 5) and ejecta of degraded craters near Ina and Ross-E-1 (see Fig. S4 of the Supplementary Material for the sampled regions) are summarized in Tables II–IV. For better comparison, the thermal physical properties (i.e., the RA [50] and H-parameter [51]) of these features are also listed. H-parameter is the e-folding depth of density increase with depth, and a low H-parameter signals high thermal inertia, potentially from decreased porosity or a higher concentration of small rock fragments (< 1 m) [14].

For visual comparison, the radar characteristics of IMPs and referenced features are depicted on a scatter plot (see Fig. 8). Noting that the backscattering coefficients of the lunar surface might follow a lognormal distribution [52], hence the median values of data in dB are reported here, and the error bar indicates a standard deviation. The variation of the median of σ_{OC}^0 versus CPR (bin width $= 0.1$) in mare regions is also displayed as a
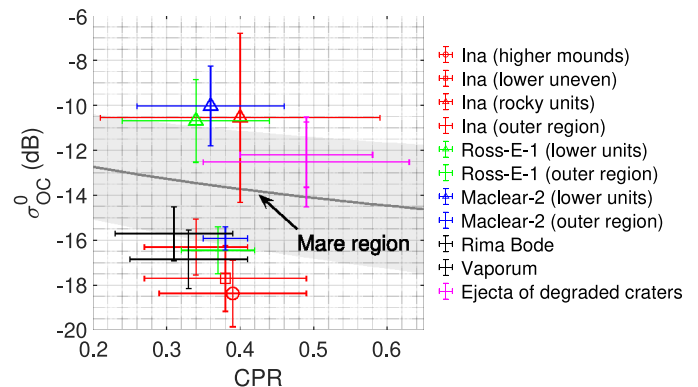

Fig. 8.　Scatter plots of σ_{OC}^0 and CPR of different terrains in different IMPs, pyroclastic deposits and ejecta of degraded craters. The averaged trend of σ_{OC}^0 varying with CPR is plotted for reference. The error bar and gray-filling region represent one std deviation.

gray line for reference, and the shadow represents one standard deviation. The Mini-RF 128 PPD global mosaic data [16] and shape files of mare boundaries provided by Nelson et al. [53] are used here. It is not surprising that there is a negative trend between σ_{OC}^0 and CPR, because a larger value of CPR indicates a stronger depolarization effect and smaller polarized-scattering power, i.e., σ_{OC}^0.

It should be careful to compare the IMPs' characteristics with the average of mare regions. The curve for the mare region is from the global mosaic data, which has a larger size of pixels ($238\,\text{m} \times 238\,\text{m}$) than the original images ($15\,\text{m} \times 30\,\text{m}$) used for

TABLE III
DFSAR RADAR CHARACTERISTICS OF INA IMP

IMP name	Terrain units	σ_{OC}^0 (dB): median±std.	CPR: median±std.	σ_{VV}^0 (dB): median±std.	σ_{HV}^0 (dB): median±std.
Ina	higher mounds	-17.70 ± 2.31	0.07 ± 0.02	-17.69 ± 2.26	-30.38 ± 0.61
	lower uneven	-16.17 ± 1.89	0.06 ± 0.02	-16.27 ± 1.82	-29.71 ± 0.50
	rocky units	-11.08 ± 2.54	0.06 ± 0.03	-11.18 ± 2.53	-24.51 ± 2.48
	outer regions	-16.46 ± 1.08	0.07 ± 0.03	-16.48 ± 1.01	-29.39 ± 0.99

characterizing IMPs. The process of averaging neighbor pixels to make global mosaics will reduce number of values at both large and small ends, hence narrowing down the value range. Therefore, it seems that most of the samples are out of the region of "average mare" (i.e., the gray region in Fig. 8). Nonetheless, IMPs are geologic features distinct from lunar maria according to their σ_{OC}^0 and CPR characteristics.

From Fig. 8, the OC scattering coefficients σ_{OC}^0 of the three radar bright IMPs (i.e., Ross-E-1, Maclear-2, and the unnamed #32) are significantly larger than those of higher mounds and lower uneven units in Ina, comparable to rocky units in Ina and the ejecta of degraded craters. Based on Table II, this observation is also consistent with that Ross-E-1 (RA = 1.70%) and Maclear-2 (RA = 1.99%) have higher RA than nonrocky units in Ina (RA of higher mounds = 0.39%, RA of lower uneven units = 0.65%) [9]. This result confirms the presence of rocks on Ross-E-1 and Maclear-2.

However, the CPR of radar bright IMPs is lower than that of the ejecta of degraded craters (ΔCPR = -0.15), noting that the ejecta is a proxy of blocky materials. The ejecta of fresh craters has even higher CPR, approaching $\sim$1.0 [54]. This difference may indicate that the large rocks on these radar-bright IMPs are sparsely distributed. The sparse rocks will increase the scattering coefficients σ_{OC}^0, but might be not enough to increase the CPR [19]. The thin, smoother fine-grained materials covering these IMPs may also contribute to the reduced CPR.

The σ_{OC}^0 of nonrocky units in Ina is slightly smaller than that of its surrounding region ($\Delta\sigma_{\mathrm{OC}}^0 = -1.90$ dB) and even the pyroclastic deposits (see Fig. 8). We interpret this as resulting from the higher mounds and lower uneven units in Ina having smoother roughness than surrounding regions at the centimeter scale. This statement is also supported by the result from LROC phase ratio images [10], [11]. Furthermore, a small normalized root-mean-square (rms) undulating height $k\delta \sim 0.2$–0.3 can optimally fit the DFSAR copolarized scattering coefficients of the nonrocky units in Ina (see Table III) with the integral equation method (IEM)-based rough surface scattering model [15], assuming that the rms slope is $3°$. This result again confirms the smoothness of the nonrocky units in Ina at the centimeter scale. In addition, the relatively low thermal inertia (as indicated by the high H-parameter in Table II) observed in the higher mounds and lower uneven units, suggesting unconsolidated materials, is consistent with the radar observation of low scattering coefficients here.

The CPR of nonrocky units in Ina is slightly higher than that of pyroclastic deposits (see Fig. 8), consistent with the observation of Carter et al. [6]. This indicates that the materials covering the higher mounds and lower uneven units in Ina comprise coarser grains when compared with the pyroclastic deposits at Rima Bode and Vaporum. Instead, the CPR of nonrocky units in Ina is comparable to that of the rocky units in Ina. It certainly does not imply the presence of rocks in higher mounds and lower uneven units in Ina, considering their exceptionally low scattering coefficients. This also suggests that relying solely on CPR parameter for assessing rockiness is unreliable.

Table II reveals that the scattering coefficients of higher mounds in Sosigenes and Cauchy-5, as well as lower uneven units in Sosigenes, are all comparable to those of nonrocky units in Ina and the pyroclastic deposits (see Table IV). This indicates that the higher mounds and lower uneven units in Sosigenes, as well as the higher mounds in Cauchy-5, are also covered by materials with low dielectric constants, similar to the nonrocky units in Ina. This low dielectric constant materials could be fine-grained regolith or highly porous lava rock. Nevertheless, as mentioned earlier and evident in Table II, the RAs in these nonrocky units in Sosigenes and Cauchy-5 are remarkably high. This is attributed to contamination in Diviner measurements from adjacent rocky units. In contrast, the sampled higher mounds in Ina are large and isolated from rocky units, resulting in RA measurements less influenced by such contamination.

IV. DISSCUSSION

In this section, we first put the observed radar characteristics of IMPs in a geologic context. Then, its implications for the origin of IMPs are discussed.

A. Higher Mounds and Lower Uneven Units

The higher mounds and lower uneven units within IMPs exhibit radar characteristics (i.e., scattering coefficients, dominant scattering mechanism and CPR) similar to the surrounding regions of their host IMPs, as well as to the fine-grained pyroclastic deposits. Hence, there might be a layer of rock-free materials that covers higher mounds and lower uneven units. At least, the RA of such a layer is lower than or comparable to that of the surrounding mare regolith.

The thickness of this rock-free materials can be roughly estimated based on the presented radar observations. The penetration depth of Mini-RF at the studied IMPs is ≥ 0.5 m (see

TABLE IV
MINI-RF RADAR CHARACTERISTICS AND THERMAL PHYSICAL PROPERTIES OF PYROCLASTIC DEPOSITS AND EJECTA OF DEGRADED CRATERS

Feature type	Feature name	σ_{oc}^0 (dB): median±std.	CPR: median±std.	RA (%)[a]	H (m)[b]
Pyroclastic depsoits	Rima Bode	-16.85 ± 1.30	0.33 ± 0.08	0.22	0.082
	Vaporum	-15.71 ± 1.20	0.31 ± 0.08	0.26	0.078
Ejecta of degraded craters	Crater in the west of Ina	-12.20 ± 1.45	0.49 ± 0.09	0.78	0.056
	Crater in the west of Ross-E-1	-12.52 ± 1.99	0.49 ± 0.14	1.16	0.055

[a,b]The RA and H values are calculated in this study based on the global RA map [50] and H-parameter map [51].

the Supplementary Material). Meanwhile, the DFSAR with a longer wavelength achieves a penetration depth of ~ 1.2 m at Ina. After propagating through the regolith for a distance equal to the radar penetration depth, the intensity of the radar waves will attenuate to $1/e$ of the initial intensity (i.e., the scattering coefficient will decrease by -4.3 dB). Here, we consider the DFSAR scattering coefficient of rocky units in Ina (see Table III) as the representative scattering coefficient for rocks, i.e., ~ -11 dB. If rocks are present beneath the rock-free materials at a depth of 0.6 m (half of the penetration depth of DFSAR), then the scattering coefficient measured by DFSAR can be -15 dB ($= -11$ dB $- 4.3$ dB). This value is still larger than that of the scattering coefficients of nonrocky units in Ina and surrounding mare regolith (< -16 dB, Table III), which means the rocks at this depth can be detected by DFSAR. Based on this analysis, the thickness of the rock-free materials can be > 0.6 m. This is a highly conservative estimate. First, the scattering coefficient of rocks may be larger than the assumed value [19]. Second, the scattering coefficients of nonrocky units in Ina might be smaller than those reported in Table III, owing to the previously mentioned impact of topography and imperfect orthorectification. Finally, employing SAR data with a longer wavelength may allow a more refined estimation of the thickness of this layer of rock-free materials. However, the available P-band Earth-based SAR data [25] is unable to achieve this due to its coarse resolution ($\sim$400 m).

What are the sources of the rock-free and fine-grained materials covering non-rocky units in IMPs? Considering the striking resemblance in radar characteristics to the surrounding mare regolith, the first explanation leans toward the "impact gardening" process. Impact gardening is the primary process responsible for generating lunar surface regolith, involving the excavation and pulverization of bedrock [22]. By using the lunar regolith evolution model proposed recently by Zhang et al. [22], to generate a layer of regolith as thick as >0.6 m, the absolute model age of Ina would have been > 250 Myr (larger than the model age of $\sim$33 Myr [2]). Therefore, the recent extrusion of lava flows without any other specific conditions for the rapid formation of regolith does not seem to explain the radar observations of IMPs. Instead, the similarity between the radar characteristics of the materials covering nonrocky units in IMPs and surrounding mare regolith may indicate that they have the same origin. In other words, the higher mounds and lower uneven units in IMPs might be as old as their host maria. This possibility is strongly

supported by the fact that some of the higher mounds in Ina are directly connected to the surrounding mare [7].

The scattering coefficients of nonrocky units in IMPs are even slightly smaller than those of the fine-grained pyroclastic deposits. Therefore, pyroclastic eruption may also play a role in producing these rock-free materials covering higher mounds and lower uneven units. Previous studies with Earth-based radar data revealed a halo of low CPR around Cauchy-5 and Hyginus crater IMPs. This observation may also suggest the eruption of fine-grained pyroclastic eruptions. Recently, Vannier et al. [55] found that the spectral of most large IMPs (e.g., Ina, Sosigenes, and Cauchy-5) indicated small additions of olivine or glass, suggesting the presence of thin and degraded pyroclastic deposits. However, this spectral feature was not observed for the small IMPs. Their findings align with the radar observations in this study, indicating that only large IMPs containing significant rock-free materials. Finally, the following 3 points all suggest that the pyroclastic deposits are generally not the primary contributors to the rock-free materials on nonrocky units in IMPs:

1) no low CPR halo is observed for Ina and Sosigenes in our study;
2) the CPR of higher mounds and lower uneven units in Ina is slightly higher than that of fine-grained pyroclastic deposits;
3) the small additions of olivine or glass as noted in the study by Vannier et al. [55].

B. Radar-Bright Units

Based on the analysis of the radar characteristics of higher mounds and lower uneven units, it is suggested that the IMPs are most likely ancient features, possibly as old as their host maria. However, the rocky units in Ina and Sosigenes, as well as the lower units on the north shield flank of Cauchy-5 and in Ross-E-1, Maclear-2, and the Unnamed #32 IMPs are all radar-bright units, indicating a lack of fine-grained materials. Therefore, if the IMPs are old, there must be a mechanism or process responsible for the removal of fine-grained materials from IMPs, preventing the accumulation of regolith generated through impact gardening.

With regard to the regolith removal in Ina, Schultz, Staid, and Pieters proposed that it might be attributed to recent outgassing [1]. However, it is puzzling why the regolith fines on higher mounds remain undisturbed. It is less likely that the regolith fines on higher mounds are redeposited after outgassing,

especially considering their thickness (>0.6 m as constrained in this study). In fact, an interesting observation in Fig. 3 is that the rocky units are mainly distributed in the peripheral regions inside Ina. This characteristic may be explained by a combination of the following factors.

1) Due to mass wasting, some of these rocks fall down from the Ina pit wall. The Ina inner wall with local slopes ranging from 5° to 15° [7] is composed of surrounding maria materials, which can possess fruitful rocks in depth. For the small sizes of these rocks, no trails behind them can be identified from available optical images. However, such rockfalls can be found at Sosigenes IMP and are prevalent on the lunar surface [11], [56].

2) Compared with its central parts, the peripheral regions in Ina have thinner regolith fines. Relatively large impacts can excavate rocks in these regions. Such examples can be found in the southern and western perimeter of the Ina depression from the enlarged NAC optical images.

3) The topography of the center of Ina is lower than its perimeter (see Fig. 1), which means that the regolith fines can migrate from the surrounding area to the middle with seismic shaking.

Different from mass wasting, the relatively gentle slopes in these regions prevented the movement of the rocks. In contrast, lighter lunar soil particles are more susceptible to migration with the force of seismic shaking [57].

Qiao et al. [3] also proposed a mechanism driven by seismic shaking force for the removal of regolith fines in Ina and other IMPs [4], [11]. In this hypothesis, the fine-grained materials on the lower units would be sifted into the voids beneath the surface (i.e., regolith drainage process), so continue exposing immature materials (e.g., rocks) in substrate. As suggested by Qiao et al. [11], this process will also result in a smoother sub-resolution roughness of IMPs. Therefore, the regolith drainage process with seismic shaking is supported by the following observations in this study.

1) Low roughness of the surface of the lower uneven units in Ina indicated by radar.

2) Presence of radar-bright IMPs (with thinner regolith and exposed rocks).

3) Low subresolution roughness of the radar-bright IMPs observed in NAC phase-ratio images.

Finally, it should be emphasized that the regolith drainage process requires a highly vesicular substrate, underscoring the presence of foamy magmas during the formation of lava crust.

C. Implications for the Origin of IMPs

Before delving into the discussion of the origin of IMPs, it is important to note that the various hypotheses regarding IMP origins are not mutually exclusive; they are proposed to explain certain characteristics of IMPs. Based on the radar observations in this study, we examine the origins of IMPs through two scenarios: younger IMPs and older IMPs.

If the IMPs are young (e.g., formed by recent extrusion of basaltic flow [2]), it is not surprising to see the radar-bright units (i.e., lower units on the north shield flank of Cauchy-5 and in radar-bright IMPs). However, a fast regolith formation mechanism (e.g., fine-grained pyroclastic eruption) must be included to account for the observed radar characteristics of higher mounds and lower uneven units in IMPs. Nevertheless, the substantial deposition of fine-grained pyroclastic material (as thick as > 0.6 m) from a recent eruption would contradict our earlier conclusion that pyroclastic deposits should not be the primary source of the rock-free materials on non-rocky units in IMPs. Therefore, this "younger IMPs" scenario is not preferred here.

If the IMPs are old (e.g., formed by ancient magmatic foam extrusion [4], [8]), then there has been sufficient time for the formation of fine-grained regolith covering nonrocky units in IMPs. However, there must be a mechanism for the ongoing removal of regolith from the lower units of IMPs, preventing the accumulation of regolith from impact gardening, in order to explain the observed radar-bright units. This mechanism for regolith removal can be either recent outgassing or regolith drainage process. Meanwhile, the presented thick regolith fines on the higher mounds, as well as the confined extents of smoothed surfaces in IMPs (evidenced by NAC phase-ratio images in radar-bright IMPs, this work; and Sosigenes [11]) provide stronger support for the regolith drainage process. This is because the outgassing process might leave trace amounts of regolith fines and also result in a diffuse extent of smoothed surface [11]. Moreover, all the three studied small IMPs (i.e., Ross-E-1, Maclear-2, and the Unnamed #32), as well as lower units on the north shield flank of Cauchy-5 are radar-bright units. It might be resonably expected that most of the other small IMPs (83 out of 91) without higher mounds are also radar-bright IMPs. If this is the case, it suggests that many outgassing events have occurred in a relatively concentrated timeframe and very recently (e.g., < 100 Myr), which seems improbable for the dormant Moon. Therefore, the regolith drainage process is preferred as the mechanism for the removal of regolith, though recent outgassing cannot be confidently excluded from available SAR data. Considering these factors, the regolith drainage process appears to be the primary driver for IMP evolution.

If the regolith drainage process plays a significant role in shaping the IMPs, then the extrusion of magmatic foam likely occurred during the initial stages of IMP formation. The magmatic foam theory predicts a porous lava crust that serves as a highly vesicular substrate facilitating the occurrence of regolith sifting. As a preliminary work, we examine the radar scattering characteristics of porous lava flows by analyzing the SAR images of Kīlauea Iki summit pit crater [see Fig. 9(a)] on the Hawai'i island, which might have vesicular lava lake crust as indicated by Qiao et al. in [3] and [12]. The full-polarimetric L-band images acquired with the airborne uninhabited vehicle SAR (UAVSAR), from the NASA Jet Propulsion Laboratory, California Institute of Technology, Pasadena, CA, USA, were used here [58]. Note that the local incident angle of UAVSAR in this crater is nearly 41°, slightly smaller than that of Mini-RF (50°). In Fig. 9(b), most parts of the floor of the crater are dark, indicating a weak radar scattering (< -20 dB). The bright regions on the floor are
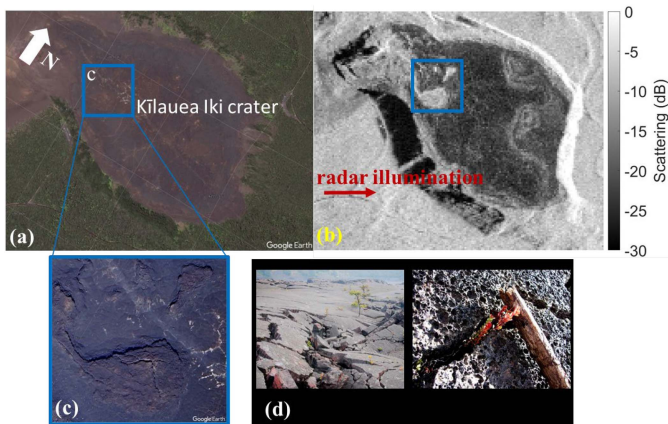
Fig. 9. Radar scattering characteristics of porous lava lake of the Kīlauea Iki summit pit crater on the Hawai'i island. (a) Optical image from Google Earth. (b) Corresponding L-band UAVSAR image (courtesy NASA/JPL-Caltech), where the (c) bright regions on its floor outlined by the blue box are cracks as zoomed out, and (d) most parts of its floor are radar dark, which are vesicular lava lake crust but with smooth surface as indicated by Qiao et al. [3].

lava flow crust cracks [see Fig. 9(c)]. The radar-dark portions of the floor also show dominantly surface scattering (i.e., dark blue in the m-chi decomposition image, but not shown here) as the lower uneven units in Ina. From the enlarged optical images [see Fig. 9(d) left], it can be seen that the surface of this lava lake crust is very smooth at the centimeter scale. The smoothness of the floor of Kīlauea Iki summit pit crater results in weakened radar scattering. This is consistent with the low-subresolution roughness of the lower uneven units in Ina and Sosigenes [10], [11]. In contrast, the radar-bright IMPs could have a very rough and rocky subsurface, but not captured by the phase-ratio images of NAC. This roughness may result from the collapse of a highly vesicular lava crust, akin to the fractures observed in the floor of Kīlauea Iki summit pit crater.

In summary, the IMPs are more likely to have formed in ancient times (e.g., extrusion of lava flow), providing sufficient time for the development of a layer of thick regolith on the higher mounds. Pyroclastic eruptions may also play a role in the generation of regolith fines in large IMPs, but they are not the main source. The existence of radar-bright IMPs suggests the presence of a mechanism for ongoing regolith removal from IMPs. The regolith drainage process offers a compelling explanation for the removal of regolith and is in accordance with radar observations.

D. Prospects for Investigating IMPs With SAR Data

In the future, more high-resolution, multifrequency, multiangle full-polarimetric SAR data are needed to provide comprehensive insights on the IMPs. These observations can provide important constraints on the magmatic foam and regolith drainage hypotheses. With multifrequency SAR data, the regolith thickness on each IMP can be well estimated. Then, conducting a systematic survey of regolith thickness in IMPs and examining its correlation with regional geological

ages can offer valuable insights into the regolith evolution on these features: How does the rate of regolith removal caused by the regolith drainage process in IMPs relative to the rate of regolith accumulation caused by impact gardening change over time? This multifrequency SAR data can be derived from high-resolution Earth-based P-band SAR [25], orbital DFSAR (S- and L-bands, [17]), and the forthcoming SAR on Chang'E-7 (L- and Ku-bands, [59]). Utilizing multiangle full-polarimetric SAR data (e.g., CE-7 SAR capable of imaging within incidence angles of 15°–45°, [59]) allows for the separation of roughness effects, enabling the inversion of the substrate porosity of the IMPs. Such a porosity information about the IMPs is crucial for testing the magmatic foam hypothesis.

V. CONCLUSION

In this study, the radar characteristics of different IMP-associated terrains are investigated and quantified by using the Mini-RF and DFSAR data. Results show that a layer of rock-poor materials (as thick as at least 0.6 m) similar to the surrounding mare regolith might exist on the top of higher mounds in Ina, Sosigenes, and Cauchy-5, as well as the lower uneven units in Ina and Sosigenes. All the studied small IMPs (i.e., Ross-E-1, Maclear-2 and the Unnamed #32) without higher mounds are radar-bright, suggesting that the regolith fines on these IMPs are extremly thin, with the underlying subsurface being notably rough and rocky. Based on the radar observations in this study, it can be concluded that: 1) if the IMPs are recently formed, there must be a mechanism for the rapid formation of regolith fines to explain the observed radar characteristics of higher mounds and lower uneven units in IMPs; 2) if the IMPs are anciently formed, there must be a mechanism for the ongoing removal of regolith from the lower units of IMPs to account for the observed radar-bright units.

Additional analysis supports the hypothesis that IMPs could have formed through ancient lava flow extrusion. Generally, pyroclastic eruptions play a limited role in regolith production in large IMPs. The regolith drainage process, coupled with seismic shaking, appears to resonably shape the radar-bright IMPs. While recent outgassing as a mechanism for regolith removal is less favored in the current findings, it cannot be definitively excluded. In the future, a systematical study on the radar characteristics of all the 91 IMPs with high-resolution, multifrequency, and multiangle full-polarimetric SAR data will provide fruitful insights into the origin and evolution of IMPs.

their work in making the TC image datasets freely available. Details about the datasets used in this study can be found in the attached supporting information.

REFERENCES

[1] P. H. Schultz, M. I. Staid, and C. M. Pieters, "Lunar activity from recent gas release," *Nature*, vol. 444, no. 7116, pp. 184–186, 2006, doi: 10.1038/nature05303.

[2] S. E. Braden, J. D. Stopar, M. S. Robinson, S. J. Lawrence, C. H. Van Der Bogert, and H. Hiesinger, "Evidence for basaltic volcanism on the moon within the past 100 million years," *Nature Geosci.*, vol. 7, no. 11, pp. 787–791, 2014, doi: 10.1038/ngeo2252.

[3] L. Qiao, J. Head, L. Wilson, L. Xiao, M. Kreslavsky, and J. Dufek, "Ina pit crater on the moon: Extrusion of waning-stage lava lake magmatic foam results in extremely young crater retention ages," *Geol.*, vol. 45, no. 5, pp. 455–458, 2017, doi: 10.1130/G38594.1.

[4] L. Qiao, J. W. Head, Z. Ling, and L. Wilson, "Lunar irregular mare patches: Classification, characteristics, geologic settings, updated catalog, origin, and outstanding questions," *J. Geophysical Res.: Planets*, vol. 125, no. 7 2020, Art. no. e2019JE006362, doi: 10.1029/2019JE006362.

[5] F. Zhang et al., "Diversity of basaltic lunar volcanism associated with buried impact structures: Implications for intrusive and extrusive events," *Icarus*, vol. 307, pp. 216–234, 2018. [Online]. Available: https://www.sciencedirect.com/science/article/pii/S0019103516306790

[6] L. M. Carter, B. R. Hawke, W. B. Garry, B. A. Campbell, T. A. Giguere, and D. B. J. Bussey, "Radar observations of lunar hollow terrain," in *Proc. 44th Lunar Planet. Sci. Conf. Houston: Lunar Planet. Inst.*, 2013, Art. no. 2146. [Online]. Available: https://www.lpi.usra.edu/meetings/lpsc2013/pdf/2146.pdf

[7] W. B. Garry et al., "The origin of INA: Evidence for inflated lava flows on the moon," *J. Geophysical Res.: Planets*, vol. 117, no. E12, 2012, doi: 10.1029/2011JE003981.

[8] L. Wilson and J. W. Head, "Eruption of magmatic foams on the moon: Formation in the waning stages of dike emplacement events as an explanation of irregular mare patches," *J. Volcanol. Geothermal Res.*, vol. 335, pp. 113–127, 2017. [Online]. Available: https://www.sciencedirect.com/science/article/pii/S0377027316303705

[9] B. D. Byron et al., "Thermophysical properties of lunar irregular mare patches from LRO diviner radiometer data," *J. Geophysical Res.: Planets*, vol. 127, no. 7, 2022, Art. no. e2022JE007214, doi: 10.1029/2022JE007214.

[10] L. Qiao, J. W. Head, L. Xiao, L. Wilson, and J. Dufek, "Sosigenes lunar irregular mare patch (IMP): Morphology, topography, sub-resolution roughness and implications for origin," in *Proc. 47th Lunar Planet. Conf. Houston: Lunar Planet. Inst.*, 2016, Art. no. 2002, [Online]. Available: https://www.hou.usra.edu/meetings/lpsc2016/pdf/2002.pdf

[11] L. Qiao, J. W. Head, L. Xiao, L. Wilson, and J. D. Dufek, "The role of substrate characteristics in producing anomalously young crater retention ages in volcanic deposits on the moon: Morphology, topography, sub-resolution roughness, and mode of emplacement of the Sosigenes lunar irregular mare patch," *Meteoritics Planet. Sci.*, vol. 53, no. 4, pp. 778–812, 2018, doi: 10.1111/maps.13003.

[12] L. Qiao et al., "Geological characterization of the INA shield volcano summit pit crater on the moon: Evidence for extrusion of waning-stage lava lake magmatic foams and anomalously young crater retention ages," *J. Geophysical Res.: Planets*, vol. 124, no. 4, pp. 1100–1140, 2019, doi: 10.1029/2018JE005841.

[13] L. Qiao, J. W. Head, L. Wilson, and Z. Ling, "The cauchy 5 small, low-volume lunar shield volcano: Evidence for volatile exsolution-eruption patterns and type 1/type 2 hybrid irregular mare patch formation," *J. Geophysical Res.: Planets*, vol. 125, no. 2, 2020, Art. no. e2019JE006171, doi: 10.1029/2019JE006171.

[14] C. M. Elder et al., "Young lunar volcanic features: Thermophysical properties and formation," *Icarus*, vol. 290, pp. 224–237, 2017. [Online]. Available: https://www.sciencedirect.com/science/article/pii/S0019103516307679

[15] W. Fa, M. A. Wieczorek, and E. Heggy, "Modeling polarimetric radar scattering from the lunar surface: Study on the effect of physical properties of the regolith layer," *J. Geophysical Res.: Planets*, vol. 116, no. E3, 2011, doi: 10.1029/2010JE003649.

[16] J. T. S. Cahill et al., "The miniature radio frequency instrument's (Mini-RF) global observations of Earth's Moon," *Icarus*, vol. 243, pp. 173–190, 2014. [Online]. Available: https://www.sciencedirect.com/science/article/pii/S0019103514003844

[17] S. S. Bhiravarasu et al., "Chandrayaan-2 dual-frequency synthetic aperture radar (DFSAR): Performance characterization and initial results," *Planet. Sci. J.*, vol. 2, no. 4, 2021, Art. no. 134, doi: 10.3847/PSJ/abfdbf.

[18] D. Putrevu, A. Das, J. G. Vachhani, S. Trivedi, and T. Misra, "Chandrayaan-2 dual-frequency SAR: Further investigation into lunar water and regolith," *Adv. Space Res.*, vol. 57, no. 2, pp. 627–646, 2016. [Online]. Available: https://www.sciencedirect.com/science/article/pii/S0273117715007486

[19] N. Liu, F. Xu, and Y. Q. Jin, "Recognition of volumetric scattering of lunar regolith media in the PSR via fully polarimetric SAR data," *IEEE J. Sel. Topics Appl. Earth Observ. Remote Sens.*, vol. 15, pp. 7657–7664, Sep. 2022, doi: 10.1109/JSTARS.2022.3204534.

[20] G. M. Wolff et al., "New fine-scale investigation of irregular mare patches," in *Proc. 54th Lunar Planet. Sci. Conf. Houston: Lunar Planet. Inst.*, 2023, Art. no. 2755. [Online]. Available: https://www.hou.usra.edu/meetings/lpsc2023/pdf/2755.pdf

[21] S. S. Bhiravarasu et al., "New L-band radar observations of ina feature on the moon," in *Proc. 54th Lunar Planet. Sci. Conf. Houston: Lunar Planet. Inst., Conf. Paper*, 2023, Art. no. 1914. [Online]. Available: https://www.hou.usra.edu/meetings/lpsc2023/pdf/1914.pdf

[22] M. Zhang, W. Fa, and V. R. Eke, "Modeling the evolution of lunar regolith: 1 formation mechanism through individual simple impact craters," *J. Geophysical Res.: Planets*, vol. 128, no. 8, 2023, Art. no. e2023JE007850, doi: 10.1029/2023JE007850.

[23] B. A. Campbell, *Radar Remote Sensing of Planet. Surfaces*. Cambridge, U.K.: Cambridge Univ. Press, 2002.

[24] B. A. Campbell, B. R. Hawke, L. M. Carter, R. R. Ghent, and D. B. Campbell, "Rugged lava flows on the moon revealed by Earth-based radar," *Geophysical Res. Lett.*, vol. 36, no. 22, 2009, doi: 10.1029/2009GL041087.

[25] B. A. Campbell et al., "Focused 70-cm wavelength radar mapping of the Moon," *IEEE Trans. Geosci. Remote Sens.*, vol. 45, no. 12, pp. 4032–4042, Dec. 2007.

[26] B. A. Campbell et al., "Earth-based 12.6-cm wavelength radar mapping of the moon: New views of impact melt distribution and mare physical properties," *Icarus*, vol. 208, no. 2, pp. 565–573, 2010. [Online]. Available: https://www.sciencedirect.com/science/article/pii/S0019103510001132

[27] S. Nozette et al., "The lunar reconnaissance orbiter miniature radio frequency (Mini-RF) technology demonstration," *Space Sci. Rev.*, vol. 150, no. 1, pp. 285–302, 2010, doi: 10.1007/s11214-009-9607-5.

[28] R. K. Raney et al., "The lunar Mini-RF radars: Hybrid polarimetric architecture and initial results," *Proc. IEEE*, vol. 99, no. 5, pp. 808–823, May 2011.

[29] J.-S. Lee and E. Pottier, *Polarimetric Radar Imaging: From Basics to Applications*. Boca Raton, FL, USA: CRC Press, 2009.

[30] R. K. Raney, J. T. S. Cahill, G. W. Patterson, and D. B. J. Bussey, "The m-chi decomposition of hybrid dual-polarimetric radar data with application to lunar craters," *J. Geophysical Res.: Planets*, vol. 117, no. E12, 2012, doi: 10.1029/2011je003986.

[31] E. J. Speyerer, M. S. Robinson, B. W. Denevi, and L. S. Team, "Lunar reconnaissance orbiter camera global morphological map of the moon," in *Proc. 42nd Lunar Planet. Sci. Conf. Houston: Lunar Planet. Inst.*, 2011, Art. no. 2387. [Online]. Available: https://www.lpi.usra.edu/meetings/lpsc2011/pdf/2387.pdf

[32] L. M. Carter, B. A. Campbell, B. R. Hawke, D. B. Campbell, and M. C. Nolan, "Radar remote sensing of pyroclastic deposits in the southern mare serenitatis and mare vaporum regions of the moon," *J. Geophysical Res.: Planets*, vol. 114, no. E11, 2009, doi: 10.1029/2009JE003406.

[33] R. L. Kirk, T. L. Becker, J. Shinaman, K. L. Edmundson, D. Cook, and D. B. J. Bussey, "A radargrammetric control network and controlled Mini-RF mosaics of the Moon's north pole...at last!," in *Proc. 44th Lunar Planet. Sci. Confe. Houston: Lunar Planet. Inst.*, 2013, Art. no. 2920. [Online]. Available: https://www.lpi.usra.edu/meetings/lpsc2013/pdf/2920.pdf

[34] V. R. Eke, S. A. Bartram, D. A. Lane, D. Smith, and L. F. A. Teodoro, "Lunar polar craters–icy, rough or just sloping?," *Icarus*, vol. 241, pp. 66–78, 2014. [Online]. Available: https://www.sciencedirect.com/science/article/pii/S0019103514003327

[35] C. P. Harris, B. J. Thomson, J. T. S. Cahill, G. W. Patterson, and R. L. Kirk, "Characterizing positional offsets in map-projected Mini-RF monostatic data," in *Proc. 53rd Lunar Planet. Sci. Conf.*, 2022, vol. 2678, Art. no. 2856. [Online]. Available: https://ui.adsabs.harvard.edu/abs/2022LPICo2678.2856H

[36] C. I. Fassett et al., "Mini-RF s-band radar observations of the moon as a function of local incidence angle," in *Proc. 54th Lunar Planet. Sci. Conf. Houston: Lunar Planet. Inst.*, 2023, Art. no. 1564. [Online]. Available: https://www.hou.usra.edu/meetings/lpsc2023/pdf/1564.pdf

[37] J. Laura et al., "Integrated software for imagers and spectrometers," *Zenodo*, 2023, doi: 10.5281/zenodo.7644616.

[38] E. Mazarico, G. A. Neumann, D. E. Smith, M. T. Zuber, and M. H. Torrence, "Illumination conditions of the lunar polar regions using LOLA topography," *Icarus*, vol. 211, no. 2, pp. 1066–1081, 2011. [Online]. Available: https://www.sciencedirect.com/science/article/pii/S0019103510004203

[39] J. Haruyama et al., "Global lunar-surface mapping experiment using the lunar imager/spectrometer on SELENE," *Earth, Planets Space*, vol. 60, no. 4, pp. 243–255, 2008, doi: 10.1186/BF03352788.

[40] M. R. Henriksen et al., "Extracting accurate and precise topography from LROC narrow angle camera stereo observations," *Icarus*, vol. 283, pp. 122–137, 2017. [Online]. Available: https://www.sciencedirect.com/science/article/pii/S001910351630152X

[41] D. Small and A. Schubert, "Guide to sentinel-1 geocoding," *Remote Sens.*, Lab. Univ. Zurich (RSL), Zürich, Switzerland, Tech. Rep. UZHS1-GC-AD, 2019.

[42] R. K. Raney, "Hybrid-polarity SAR architecture," *IEEE Trans. Geosci. Remote Sens.*, vol. 45, no. 11, pp. 3397–3404, Nov. 2007.

[43] Y. Yamaguchi *Polarimetric SAR Imaging: Theory and Applications*. Boca Raton, FL, USA: CRC Press, 2020.

[44] C. Deledalle, L. Denis, F. Tupin, A. Reigber, and M. Jäger, "NL-SAR: A unified nonlocal framework for resolution-preserving (Pol)(In)SAR denoising," *IEEE Trans. Geosci. Remote Sens.*, vol. 53, no. 4, pp. 2021–2038, Apr. 2015.

[45] Y. Gao et al., "Investigating the dielectric properties of lunar surface regolith fines using Mini-RF SAR data," *ISPRS J. Photogrammetry Remote Sens.*, vol. 197, pp. 56–70, 2023. [Online]. Available: https://www.sciencedirect.com/science/article/pii/S092427162300014X

[46] B. A. Campbell, "High circular polarization ratios in radar scattering from geologic targets," *J. Geophysical Res.: Planets*, vol. 117, no. E6, 2012, doi: 10.1029/2012JE004061.

[47] N. Liu, F. Xu, and Y. Q. Jin, "A numerical model of CPR of rough surface with discrete scatterers for analysis of Mini-RF data," *Radio Sci.*, vol. 55, no. 5, pp. 1–11, 2020, doi: 10.1029/2018RS006776.

[48] N. Liu and Y. Q. Jin, "Simulation of Pol-SAR imaging and data analysis of Mini-RF observation from the lunar surface," *IEEE Trans. Geosci. Remote Sens.*, vol. 60, Mar. 2021, Art. no. 2000411, doi: 10.1109/TGRS.2021.3064091. [Online]. Available: https://ieeexplore.ieee.org/document/9387452/

[49] V. Kaydash, Y. Shkuratov, and G. Videen, "Phase-ratio imagery as a planetary remote-sensing tool," *J. Quantitative Spectrosc. Radiative Transfer*, vol. 113, no. 18, pp. 2601–2607, 2012. [Online]. Available: https://www.sciencedirect.com/science/article/pii/S0022407312001434

[50] J. L. Bandfield, R. R. Ghent, A. R. Vasavada, D. A. Paige, S. J. Lawrence, and M. S. Robinson, "Lunar surface rock abundance and regolith fines temperatures derived from LRO diviner radiometer data," *J. Geophysical Res.: Planets*, vol. 116, no. E12, 2011, doi: 10.1029/2011JE003866.

[51] P. O. Hayne et al., "Global regolith thermophysical properties of the Moon from the diviner lunar radiometer experiment," *J. Geophysical Res.: Planets*, vol. 122, no. 12, pp. 2371–2400, 2017, doi: 10.1002/2017JE005387.

[52] W. Fa and M. A. Wieczorek, "Regolith thickness over the lunar nearside: Results from Earth-based 70-cm Arecibo radar observations," *Icarus*, vol. 218, no. 2, pp. 771–787, 2012. [Online]. Available: https://www.sciencedirect.com/science/article/pii/S0019103512000255

[53] D. M. Nelson et al., "Mapping lunar maria extents and lobate scarps using LROC image products," in *Proc. 45th Lunar Planet. Sci. Conf. Houston: Lunar Planet. Inst.*, 2014, Art. no. 2861. [Online]. Available: https://www.hou.usra.edu/meetings/lpsc2014/pdf/2861.pdf

[54] W. Fa and V. R. Eke, "Unravelling the mystery of lunar anomalous craters using radar and infrared observations," *J. Geophysical Res: Planets*, vol. 123, no. 8, pp. 2119–2137, 2018, doi: 10.1029/2018JE005668.

[55] H. Vannier, B. Horgan, and J. Stopar, "Investigating 16 irregular mare patches with visible/near-infrared spectra from the moon mineralogy mapper," in *Proc. 53rd Lunar Planet. Sci. Conf. Houston: Lunar Planetary Inst.*, 2022, Art. no. 2311. [Online]. Available: https://www.hou.usra.edu/meetings/lpsc2022/pdf/2311.pdf

[56] V. T. Bickel, J. Aaron, A. Manconi, S. Loew, and U. Mall, "Impacts drive lunar rockfalls over billions of years," *Nature Commun.*, vol. 11, no. 1, 2020, Art. no. 2862, doi: 10.1038/s41467-020-16653-3.

[57] Z. Xiao, Z. Zeng, N. Ding, and J. Molaro, "Mass wasting features on the Moon–how active is the lunar surface?," *Earth Planet. Sci. Lett.*, vol. 376, pp. 1–11, 2013. [Online]. Available: https://www.sciencedirect.com/science/article/pii/S0012821X13003312

[58] S. Hensley et al., "The UAVSAR instrument: Description and first results," in *Proc. IEEE Radar Conf.*, 2008, pp. 1–6.

[59] Y. Wang et al., "Lunar microwave imaging radar (LMIR)," in *Proc. 14th Eur. Conf. Synthetic Aperture Radar*, Leipzig, Germany, 2022, pp. 1–3.

Fei Zhao received the B.E. degree in electronic information engineering from the University of Chinese Academy of Sciences, Beijing, China, in 2020. He is currently working toward the Ph.D. degree with the National Key Laboratory of Microwave Imaging Technology, Aerospace Information Research Institute, Chinese Academy of Sciences, Beijing, China.

His research interests include modeling the microwave scattering behavior of natural terrains, designing methods for processing planetary remote sensing data, and revealing the lunar surface geologic processes.

Yao Gao received the B.S. degree in electronic science and technology from Zhengzhou University, Zhengzhou, China, in 2018, and the Ph.D. degree in communication and information systems from the Aerospace Information Research Institute, Chinese Academy of Sciences, Beijing, China, in 2023.

His research interests include investigating the surface properties, tectonics, and volcanism on the terrestrial bodies using radar remote sensing techniques.

Yanan Dang received the B.S degree in geographic information system from Jilin University, Changchun, China, in 2009, and the Ph.D degree in space information technology from Macau University of Science and Technology (MUST), Macau, China, in 2019.

From 2019 to 2021, she was a Postdoctoral Researcher with State Key Laboratory of Lunar and Planetary Sciences, MUST. She is currently an Assistant Research Fellow with the National Key Laboratory of Microwave Imaging Technology, Aerospace Information Research Institute, Chinese Academy of Sciences, Beijing, China. Her research interests include comparative planetary geology, lunar SAR image interpretation, and deep space exploration.

Pingping Lu (Member, IEEE) was born in Henan, China, in 1989. She received the Ph.D. degree in communication and information systems from the Institute of Electronics, Chinese Academy of Sciences, Beijing, China, in 2016.

She was a Postdoctoral Researcher with the Department of Mechanical Engineering, University of Michigan, Ann Arbor, MI, USA, from 2018 to 2022. She is currently an Associate Research Fellow with the National Key Laboratory of Microwave Imaging Technology, Aerospace Information Research Institute, Chinese Academy of Sciences. Her research interests include synthetic aperture radar image interpretation, intelligent environment sensing, and deep space exploration.

Tingyu Meng (Associate Member, IEEE) received the B.S. degree in remote sensing science and technology from Wuhan University, Wuhan, China, in 2018, and the Ph.D. degree in cartography and geographic information systems from Aerospace Research Institute, Chinese Academy of Sciences (AIRCAS), Beijing, China, in 2023.

She is a Research Associate with the National Key Laboratory of Microwave Imaging Technology, AIRCAS. Her research interests include marine remote sensing, SAR applications in lunar exploration, and modeling of electromagnetic scattering.

Tianyuan Yang received the Ph.D. degree in signal and information processing from the National Laboratory of Radar Signal Processing, Xidian University, Xi'an, China, in 2022.

From 2020 to 2022, he was a Visiting Ph.D. Student with the University of Naples Federico II, NA, Italy. He is currently an Assistant Research Scientist with the National Key Laboratory of Microwave Imaging Technology, Aerospace Information Research Institute, Chinese Academy of Sciences, Beijing, China. His research interests include compressed sensing on radar, sparse frequency recovery, synthetic aperture radar, and inverse synthetic aperture radar.

Robert Wang (Senior Member, IEEE) received the B.S degree in control engineering from the University of Henan, Kaifeng, China, in 2002, and the Dr. Eng. degree from the Graduate University of Chinese Academy of Sciences, Beijing, China, in 2007.

In 2007, he joined the Center for Sensor Systems (ZESS), University of Siegen, Siegen, Germany. He was involved in various joint projects supported by ZESS and Fraunhofer-FHR, Wachtberg, Germany, e.g., the TerraSAR-X/phased array multifunctional imaging radar (PAMIR) hybrid bistatic synthetic aperture radar (SAR) experiment, the PAMIR/stationary bistatic SAR experiment, the PAMIR/stationary bistatic SAR experiment with nonsynchronized oscillator, and the millimeter-wave frequency-modulated continuous-wave (FMCW) SAR data processing. Since 2011, he has been a Research Fellow with the Spaceborne Microwave Remote Sensing System Department, Institute of Electronics, Chinese Academy of Sciences, Beijing, where he has been funded by the Hundred Talents Program of the Chinese Academy of Sciences. Since 2012, he has been a Co-Principal Investigator (PI) with the Helmholtz-CAS Joint Research Group, Beijing, concerning spaceborne microwave remote sensing for prevention and forensic analysis of natural hazards and extreme events. He is also responsible for several national highresolution spaceborne imaging radar missions supported by the National High- Resolution Earth Observation Major Special Program. He is also the PI of two advanced L-band spaceborne SAR systems that are aimed at global dynamic earth monitoring. He has authored or coauthored more than 100 peer-reviewed journal articles in the field of SAR imaging technology, and has authored or coauthored the book *Bistatic SAR System and Signal Processing Technology* (Springer). His research interests include monostatic and multistatic SAR imaging and high-resolution wide-swath spaceborne SAR systems and imaging models.

Dr. Wang was the recipient of the National Ten Thousand Talent Program—Young Top-Notch Talent Program Award in 2014, the National Natural Science Funds of China for Excellent Young Scholar in 2014, the Zhao Jiuzhang Award for Outstanding Young Science in 2015, the First Prize for Military Scientific and Technological Progress in 2016, the Scientific and Technological Innovation Leading Talent by National High-Level Talents Special Support Plan in 2017, and the Distinguished Young Scholars from the National Natural Science Foundation of China in 2018. He was the Session Chair at the European Conference on Synthetic Aperture Radar (EUSAR) and the International Geoscience and Remote Sensing Symposium (IGARSS) from 2012 to 2016. He has contributed to invited sessions at the EUSAR from 2008 to 2016, the European Radar Conference in 2009, and IGARSS from 2012 to 2016. He has been an Associate Editor of IEEE TRANSACTIONS ON GEOSCIENCE AND REMOTE SENSING since 2020.